ACS OMEGA

http://pubs.acs.org/journal/acsodf

Article

Tensile Mechanical Behavior and the Fracture Mechanism in Monolayer Group-III Nitrides XN (X= Ga, In): Effect of Temperature and Point Vacancies

A. S. M. Jannatul Islam, Md. Sherajul Islam,* Md. Sayed Hasan, Md. Shahadat Akbar, and Jeongwon Park

Cite This: *ACS Omega* 2022, 7, 14678−14689

Read Online

ACCESS | Metrics & More | Article Recommendations | Supporting Information

ABSTRACT: In this study, we have thoroughly investigated the tensile mechanical behavior of monolayer XN (X = Ga, In) using molecular dynamics simulations. The effects of temperature (100 to 800 K) and point vacancies (PVs, 0.1 to 1%) on fracture stress, strain, and elastic modulus of GaN and InN are studied. The effects of edge chiralities on the tensile mechanical behavior of monolayer XN are also explored. We find that the elastic modulus, tensile strength, and fracture strain reduce with increasing temperature. The point defects cause the stress to be condensed in the vicinity of the vacancies, resulting in straightforward damage. On the other hand, all the mechanical behaviors such as fracture stress, elastic modulus, and fracture strain show substantial anisotropic nature in these materials. To explain the influence of temperature and PVs, the radial distribution function (RDF) at diverse temperatures and potential energy/atom at different vacancy concentrations are calculated. The intensity of the RDF peaks decreases with increasing temperature, and the presence of PVs leads to an increase in potential energy/atom. The current work provides an insight into adjusting the tensile mechanical behaviors by making vacancy defects in XN (X = Ga, In) and provides a guideline for the applications of XN (X = Ga, In) in flexible nanoelectronic and nanoelectromechanical devices.

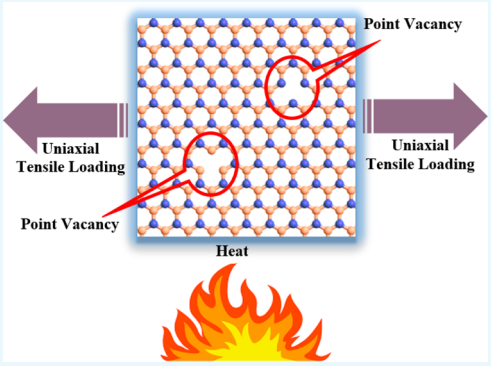

1.0. INTRODUCTION

The functional efficiency of nanodevices and nanoelectromechanical systems (NEMS) is greatly affected by the mechanical behavior of the constituent materials.[1,2] Due to the rapid shrinking trend of nanoscale devices, structural failure problems have increased considerably and must be solved urgently to realize reliable and efficient NEMS.[3] Since the exfoliation of graphene,[4,5] the very first two-dimensional (2D) materials with a honeycomb structure, a new milestone has been achieved to solve the failure problems of NEMS by using the extraordinary mechanical strength of graphene.[6,7] However, the zero electronic band gap of graphene[5] is a major limitation in all of these prospects and triggered the scientists to invent other monolayer systems with comparable behavior like graphene. Recently, monolayer group III-nitrides XN (X = Ga, In) have shown promising potential in nanoscale device fabrication owing to their outstanding electronic, piezoelectric, optical, thermal, and mechanical properties.[8−12] Although the fabrication of monolayer XN from its bulk counterpart was a great challenge, recently, using the graphene encapsulation technique and molecular beam epitaxy method, the experimental fabrication of monolayer XN has been done.[13−16] Moreover, employing a surface-confined nitridation technique, micrometer-sized 2D-GaN has been synthesized recently.[17,18] InN-based nanostructures[19,20] are also improving day by day. Therefore, the application prospects of monolayer XN in the field of NEMS such as nanoenergy harvesting, energy storage, sensing, and piezotronics are exciting, and the investigation of the mechanical properties at different circumstances attracts great attention.

Usually, the mechanical behavior of nanoscale materials is significantly influenced by the temperature of the environment and structural chirality.[7,21] Mechanical behavior of various 2D materials, including graphene, graphynes, 2D-ZnS, 2D-SiC, and $MoSe_2$,[21−26] has recently been investigated at different temperatures. The atomic vibration of nanostructures increases significantly as the system temperature increases, making the materials less stiff. Therefore, the breaking of the nanostructure may occur at an early stage and show a decreasing trend of the mechanical properties with increasing temperature. In addition, the honeycomb arrangement of 2D materials produces two types of chirality: armchair and zigzag chiralities. Hence, when a uniaxial loading is applied to nanosheets such

Received: December 23, 2021
Accepted: April 8, 2022
Published: April 18, 2022

https://doi.org/10.1021/acsomega.1c07259
ACS Omega 2022, 7, 14678−14689

as graphene, 2D-SiC, 2D-ZnS, and 2D-SiGe, the two different chiral directions of these materials show a significant dissimilar (anisotropic) mechanical strength due to changes in the bonding arrangement.[21,22,24] Conversely, due to the complex synthesizing techniques, when a monolayer structure is produced experimentally or used in different technological applications under different environmental and operating conditions, the appearance of point vacancies (PVs) such as structural defects is inevitable.[27−31] The law of thermodynamics reveals that a small amount of vacancy such as imperfections in nanoscale materials has a substantial effect on the physical properties and hence can reduce the fracture strength of the nanoscale material greatly as a result of their robust regularity breakdown effect.[32] In recent times, the effect of vacancy type defects on the fracture behavior of hybrid graphene-boron nitride, MoS_2, 2D-ZnS, and 2D-BeO has been investigated[22,33−35] It has been discovered that vacancy-induced structures fracture at breaking stress that is far lower than the intrinsic strength of ideal structures, and increasing the vacancy concentration can significantly reduce fracture stress, elastic modulus, and fracture strain. To fulfill the large-scale industrial objectives, especially at high temperatures under which the device works or considering the realistic experimental conditions with vacancy like structural defects, exploring the dependency of mechanical properties of XN is a matter of concern to avoid structural damage.

Of late, numerous experimental, as well as theoretical, investigations have been accomplished on monolayer XN to explore different physical properties such as strain- and doping-induced electronic, optical, and vibrational properties, gas molecules' adsorption behavior, excitonic properties and magnetic properties, light-harvesting behavior, topological phase transition, thermodynamic stability, and hydrogenation behaviors.[36−42] Moreover, a van der Waals heterobilayer built by XN has also been explored recently.[20] From these studies, it has been found that monolayer XN is very much promising and can be successfully employed in different piezoelectric, optoelectronic, photocatalytic, and sensing applications. Although most of the existing works has focused on studying the structural, electronic, and optical properties of XN, to the greatest of our understanding no studies have reported on the tensile mechanical behavior of this prospective monolayer. The mechanical properties of XN with different concentrations of PV along with different chiral alignments are still unknown. It is also unidentified how temperature changes affect the tensile mechanical characteristics and fracture behavior of the XN monolayer. To design reliable nanodevices and NEMS based on XN, an exhaustive investigation of their mechanical behavior is thus significantly imperative under diverse boundary conditions.

In this study, we have carried out a systematic and rigorous investigation on the tensile mechanical properties of monolayer XN through molecular dynamics (MD) simulation. Modified embedded atom method (MEAM) potential proposed by Do et al.[43] is used to explain the atomistic interaction of the considered nitride structures. We investigated the effect of temperature ranging from 100 to 800 K and PV defects with a concentration varying from 0.1 to 1.0% on the fracture performance under tensile loading along the two chiral directions. Due to the bonding properties, tensile mechanical properties such as fracture stress, elastic modulus, and fracture strain exhibit substantial anisotropic behavior for this monolayer XN. To explain the effect of temperature and PV, the radial distribution function (RDF) at different temperatures and potential energy/atom at different vacancy concentrations are calculated. The sheet deformation profile is also analyzed by considering different temperatures as well as various PV concentrations.

2.0. SIMULATION DETAILS

We used classical MD simulations to calculate the tensile mechanical characteristics of monolayer XN. The potential used in the system has a significant impact on the accurate prediction of material properties in MD simulations. Choosing a suitable potential for a particular system is thus an essential prerequisite for getting reliable results from MD simulation. Of late, Do et al.[43] developed a modified embedded-atom method (MEAM) potential for modeling the atomistic interactions between the atoms of GaN and InN in MD simulations. This potential has been shown to accurately characterize the structural, defect, and elastic properties of zinc-blende and wurtzite GaN and InN. The cohesive energy (E_C), lattice parameters (a and c), internal structural parameter (u), elastic constants (C_{11}, C_{12}, C_{13}, C_{33}, C_{44}, and C_{66}), and bulk modulus (B) of GaN and InN systems reported from the MEAM potential in the MD simulation agree well with the experimental results as well as the first-principles (FP) calculations.[43] Tables S1 and S2 (Supporting Information) show the comparison of different physical parameters of XN (X = Ga, In) reported by the MEAM potential in the MD simulation along with experimental values and FP calculations.[43] The tensile mechanical strength of monolayer XN under uniaxial tensile loading can be explored by the virial stress theorem, which can be specified as[44]

$$\sigma_{\text{virial}}(r) = \frac{1}{\Omega}\sum_i \left[\left(-m_i \dot{u}_i \otimes \dot{u}_i + \frac{1}{2}\sum_{j\neq i} r_{ij} \otimes f_{ij}\right)\right] \quad (1)$$

where the total sum is chosen for all the atoms in the volume, m_i signifies the mass of atom i, $\dot{u}_i$ signifies the time derivative of the interchange, r_{ij} signifies the location vector, and f_{ij} signifies the interatomic force applied on atom i by atom j.

Realization of single-layer XN along with two ultimate chiral alignments, namely the armchair and the zigzag directions, is exposed in Figure 1a. The dimensions considered for the monolayer GaN and InN were ∼1252.91 nm^2 (35.9 nm × 34.9 nm) and ∼1245.84 nm^2 (34.6 nm × 35.6 nm), respectively. The bond lengths for Ga−N and In−N were 1.87 and 2.06 Å, respectively. The total atoms considered in the GaN and InN sheets were 27648 and 22400, respectively. With the purpose of removing the size effect, periodic boundary conditions (PBC) were applied along the two (X and Y) orientations. An outsized vacuum space of 20 Å was taken on both faces (along the Z-axis direction) of the sheet so that the atoms do not interact along the vertical orientation, and only single-layer XN was involved in the simulation. The conjugate gradient scheme was used for the energy optimization of the structure. The finishing tolerance for force and energy were chosen as 10^{-8} eV/Å and 10^{-8}, respectively. In the optimization process, the maximum force/energy costing and the highest iterations of the minimizer were taken as 10,000 and 5000, respectively. As soon as one of the stopping criteria is fulfilled, the iteration process of minimization changed to the finishing condition. After finishing the energy optimization, an equilibration computation for 50 ps is used by means of an NVE

https://doi.org/10.1021/acsomega.1c07259
ACS Omega 2022, 7, 14678−14689

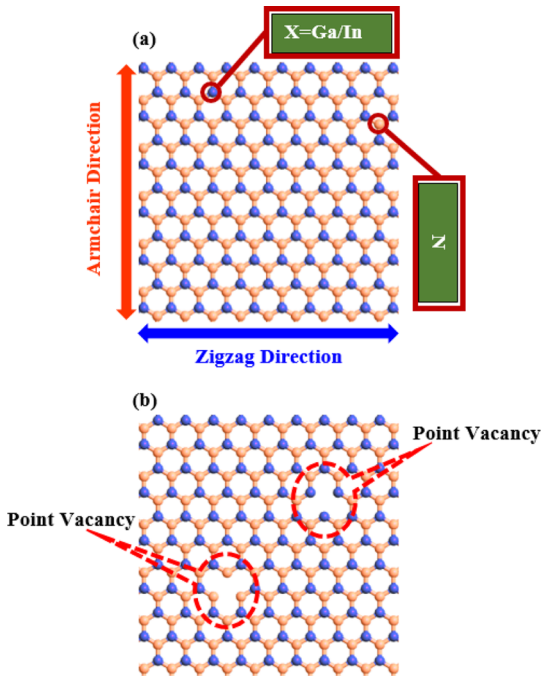

Figure 1. (a) Realization of single-layer XN (X = Ga, In) along with two fundamental chiral orientations, namely the armchair and the zigzag orientations. (b) PV defects in single-layer XN.

microcanonical ensemble. An NPT ensemble (isobaric, isothermal) for 50 ps was further utilized to equilibrate the structure pressure to 1 bar. Throughout the NPT ensemble simulation, the structure gets reorganized and all the interior pressure grown was removed. Finally, we engaged the NVT ensemble (canonical) for 30 ps for thermal easing. The equation of motion was resolved through the velocity−verlet integration method by means of a time step of 1 fs. We have utilized a stable strain rate of 10^9 s^{-1} along the tensile distortion alignments (zigzag and armchair). Although the operating strain rate is quite high, the applied strain rate is well suited for atomistic computations to determine material fracture performance with a reasonable computational expense.[21,25] For postprocessing and verifying the estimated stress, strain, and trajectories of the studied configuration, the open-source visualization software OVITO was utilized throughout the study.[45] Besides, it is well known that the trajectory of classical MD computations is enormously stochastic. To account for stochasticity and ambiguity, all MD simulations were run for four different initial conditions (i.e., molecular velocity) for both pristine and vacancy-induced configurations.[35] We took the average of the four results of these four distinct calculations to carry out the error calculation.

3.0. RESULTS AND DISCUSSION

XN (X = Ga, In) are projected to be competitive nanomaterials for real-world applications in which the environment is likely to change dramatically. Predominantly, the steadiness of the XN-based devices and systems at extreme temperatures[46−50] is a serious disquiet in current nanoelectronics. NEMS, nanosensors, nanodevices, aerospace applications, fuel-cell applications, energy-harvesting systems, and nanoactuators demand extremely durable structures at high temperatures.[7,25,26] Therefore, characterization of the fracture behavior of XN at high temperatures is very essential to employ it in the next-generation NEMS and nanoelectronics. We have thus first calculated the temperature (100 to 800 K) effect on the uniaxial tensile mechanical properties of monolayer XN. The stress−strain behavior of GaN and InN monolayers is represented in Figures 2a,b and 3a,b, respectively. For both

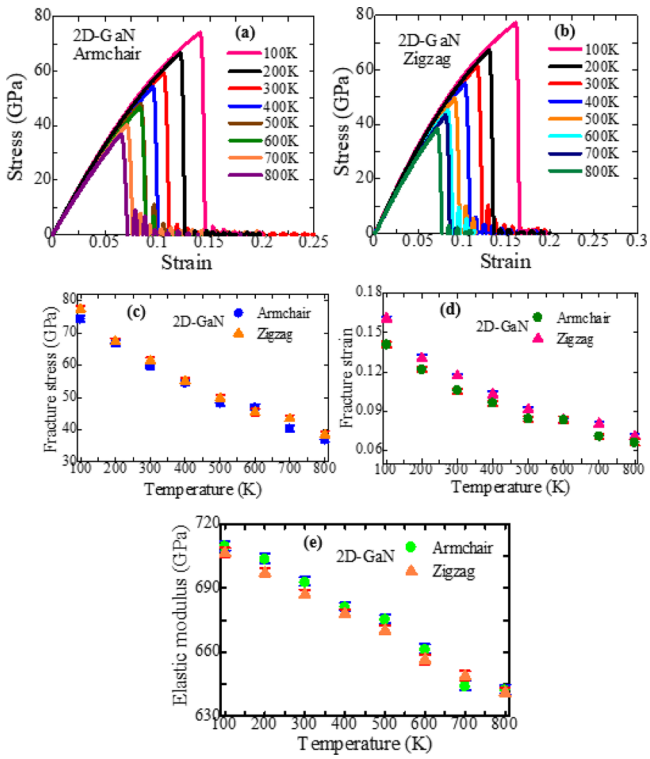

Figure 2. Effect of temperature on the stress−strain performance of single-layer GaN along the (a) armchair and (b) zigzag orientations. Temperature-dependent (c) fracture stress, (d) fracture strain, and (e) elastic modulus of single-layer GaN along the two different chiral orientations.

monolayers, the stress−strain performance maintains a linear relationship up to the fracture strain and then shows a sharp breaking, indicating that monolayer XN can show brittle types of fracture for both chiral orientations. Most importantly, with increasing temperature, a decreasing trend of the fracture stress in both the armchair and zigzag alignment is perceived for both of these GaN and InN monolayers. The thermal vibration of atoms leads the structure to become less stiff as the temperature increases. As a result, chemical bonds among the atoms are more likely to reach the acute bond length and therefore break. Two energy factors contribute to the overall energy of the uniaxial tensile deformation process when it breaks: thermal energy and strain energy. The thermal energy contribution increases linearly with temperature and therefore the required strain energy contribution for breaking the structure decreases as the temperature increases. For the GaN monolayer, at 100 K, the maximum tensile strengths of ∼74.21 and ∼77.36 GPa are found along the armchair and zigzag directions, respectively. Nevertheless, when the temperature is elevated to 800 K, the tensile strength drops from ∼74.21 to ∼36.80 GPa and from ∼77.36 to ∼38.41 GPa in the armchair and zigzag alignments, respectively. Moreover, for the InN monolayer, at a temperature of 100 K, we have found maximum tensile strengths of ∼47.38 and ∼50.26 GPa along

https://doi.org/10.1021/acsomega.1c07259
ACS Omega 2022, 7, 14678−14689

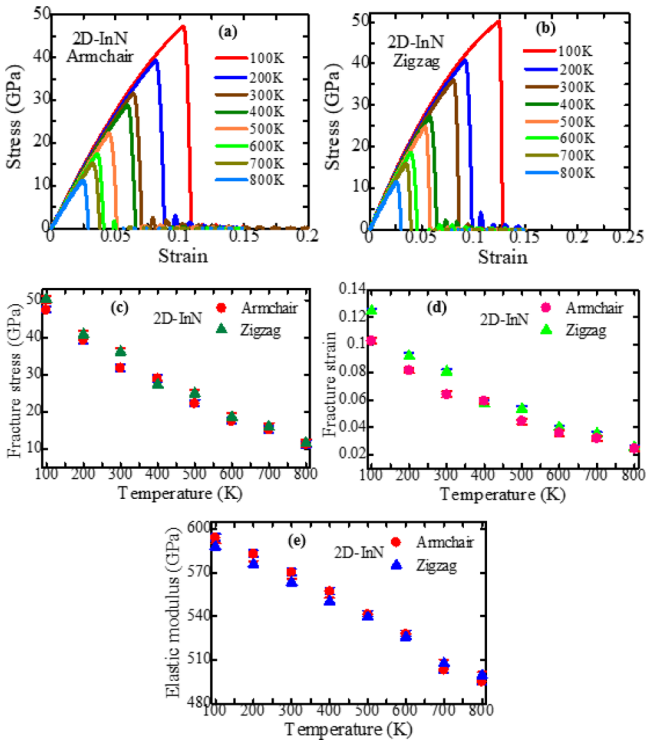

Figure 3. Effect of temperature on the stress−strain performance of single-layer InN along the (a) armchair and (b) zigzag orientations. Temperature-dependent (c) fracture stress, (d) fracture strain, and (e) elastic modulus of single-layer InN along the two different chiral orientations.

the armchair and zigzag directions, respectively. However, when the temperature of the GaN monolayer is increased to 800 K, the tensile strength is found to be ∼11.70 and ∼11.62 GPa in the armchair and zigzag directions, respectively. Similar to fracture stress, fracture strain also shows a reducing trend for both orientations of XN. At a temperature of 100 K, the fracture strains of GaN for armchair and zigzag coordinations are found to be 0.1408 and 0.1608, respectively, whereas those quantities are diminished to 0.0659 and 0.0707, respectively, once the temperature is increased to 800 K. Similarly, for the InN sheet, at 100 K, the fracture strains for armchair and zigzag alignments are 0.1028 and 0.1245, respectively, while those values are lowered to 0.0246 and 0.0254, respectively, when the temperature is increased to 800 K. The influence of temperature on the reduction of fracture stress and strain of monolayer XN for both chiral orientations is plotted in Figures 2c,d and 3c,d, respectively. Moreover, the percentage reduction of distinct mechanical properties of XN with respect to 100 K is presented in Tables S3 and S4 (Supporting Information).

Next, we have calculated the elastic modulus of XN at different temperatures. In order to calculate the elastic modulus, the stress−strain relationship is matched with a straight line considering a tiny strain of ≤2%. The smaller strain region is considered so that the structure guarantees linear elastic deformation and conforms to Hooke's law. The estimated elastic modulus of XN at diverse temperatures is depicted in Figures 2e and 3e, respectively. Identical to the tensile stress and strain, the computed elastic modulus also demonstrates a reducing nature with a higher temperature. As depicted in Figures 2e and 3e, because of the increase in temperature from 100 to 800 K, the elastic modulus of GaN

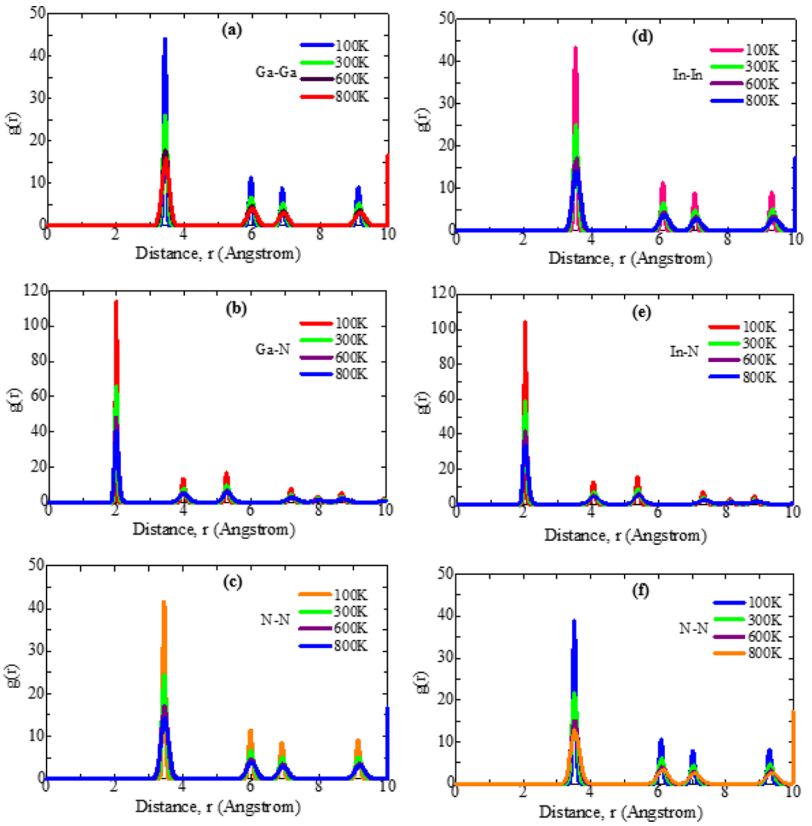

Figure 4. RDF, $g(r)$ of (a) Ga−Ga, (b) Ga−N, and (c) N−N pairs of the GaN sheet and (d) In−In, (e) In−N, and (f) N−N pairs of the InN sheet at four different temperatures.

https://doi.org/10.1021/acsomega.1c07259
ACS Omega 2022, 7, 14678−14689

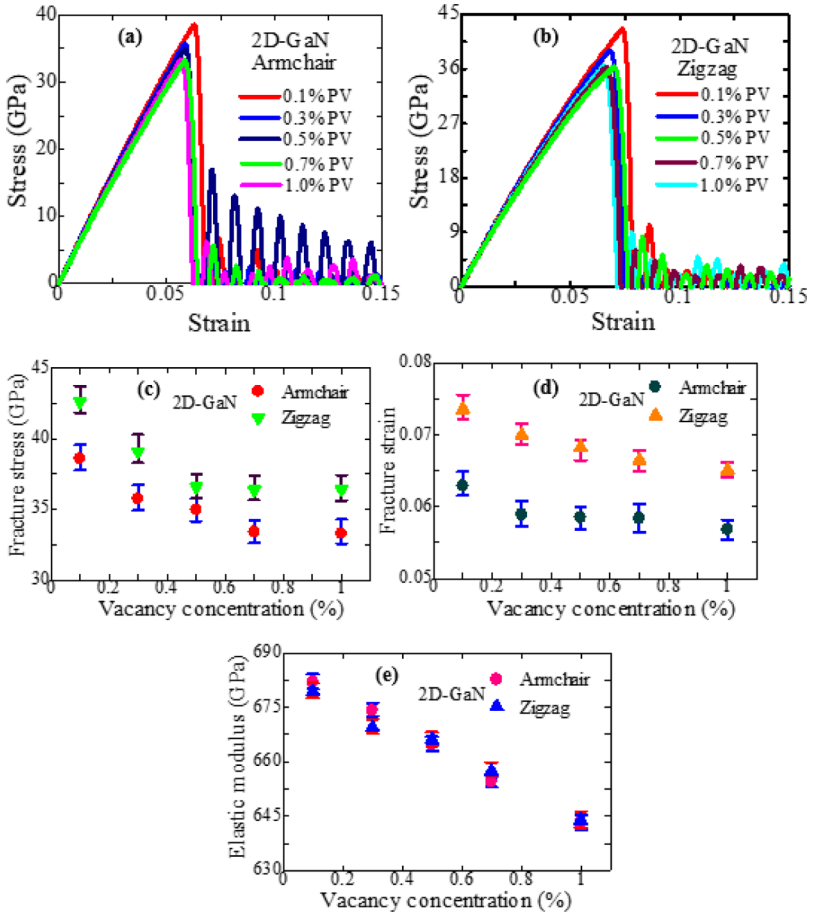

Figure 5. Stress−strain performances of PV-induced GaN sheets at 300 K along the (a) armchair and (b) zigzag orientations. PV-induced (c) fracture stress, (d) fracture strain, and (e) elastic modulus of a GaN sheet along the two different chiral orientations.

shows a reduction from ∼709.39 to ∼642.19 GPa with a ∼9.47% decrease and ∼706.42 to ∼641.05 GPa with a ∼9.25% decrease along the armchair and zigzag orientations, respectively. Conversely, because of the increase in temperature from 100 to 700 K, the elastic modulus of InN shows a reduction from ∼593.92 to ∼494.9 GPa with a ∼16.67% decrease and ∼587.71 to ∼499.47 GPa with a ∼15.02% decrease along the armchair and zigzag orientations, respectively. Hence, it can be argued that the elastic modulus of 2D-InN is more susceptible to temperature changes compared to those of 2D-GaN. The attained temperature-dependent elastic modulus agrees well with the findings of 2D-SiC, 2D-ZnS, and 2D-BeO.[21,22,35] Moreover, the elastic modulus of both GaN and InN monolayers exhibits a significant anisotropy in the armchair and zigzag alignments. The anisotropic elastic modulus behavior of XN in both chiral directions is caused by differences in bond alignments and bond stretching. Similar anisotropic elastic modulus behavior of XN was seen in ab initio calculations,[10] where the reported elastic modulus for GaN was found to be 106.586 and 105.846 N/m, respectively, in the armchair and zigzag directions. In addition, the values for InN were 61.619 and 62.158 N/m, respectively.

To explain the temperature-dependent mechanical behavior qualitatively, we have calculated the RDF at four different temperatures. The temperature-dependent RDFs of GaN (Ga−Ga, Ga−N, and N−N) and InN (In−In, In−N, and N−N) for different nearest neighbors are presented in Figure 4a−c and 4d−f, respectively. Generally, for a single-layer configuration, the RDF can be quantified as, $g_{PQ}(r) = \Delta n_{PQ}/2\pi r\Delta r\rho_Q$, where $g_{PQ}(r)$ represents the RDF, ρ_Q denotes the mean density of particles Q in the whole structure, and Δn_{PQ} denotes the mean quantity of particles of category Q present in the annular zone between r and $r + \Delta r$ with a P particle at the focus. The RDF should be a delta-like function at 0 K. However, the particles become energetic and start to oscillate from their normal location with the increase of temperature.

Consequently, the probability of finding a specific atom in the vicinity of the reference atom decreases with increasing temperature. Therefore, the RDFs show widening delta functions with decreasing peak intensities for all neighbors, indicating greater atomic vibrations and confirming the weak mechanical strength at high temperatures.[22] From Figure 4a−c, it is also noticed that the peak locations of the first, second, and third neighbors of the 2D-GaN sheet are approximately at 1.985, 3.445, and 3.455 Å, respectively, justifying the accuracy of the RDF calculations for 2D-GaN. Moreover, the peak positions of the first, second, and third neighbors of the 2D-InN sheet (Figure 4d−f) are at 2.025, 3.505, and 3.515 Å, respectively, further justifying the validity of the RDF calculations for 2D-InN.

The experimental creation of perfect nanostructures is practically unattainable. Various vacancy-like defects are formed during the production and can have unpredicted effects on the mechanical strength of nanoscale matters. Among the diverse vacancy defects, PVs, or the missing of a

https://doi.org/10.1021/acsomega.1c07259
ACS Omega 2022, 7, 14678−14689

single atom in the structure at a distinct location, is more conquerable and has a strong effect on the physical properties due to its higher symmetry breakdown effect. Moreover, PVs can be utilized as an excellent means to regulate the physical performance of monolayer XN. In this section, the impact of PVs on the mechanical strength of single-layer XN under uniaxial tensile loading at 300 K is investigated. Figures 5a,b and 6a,b demonstrate the stress−strain behavior of PV-

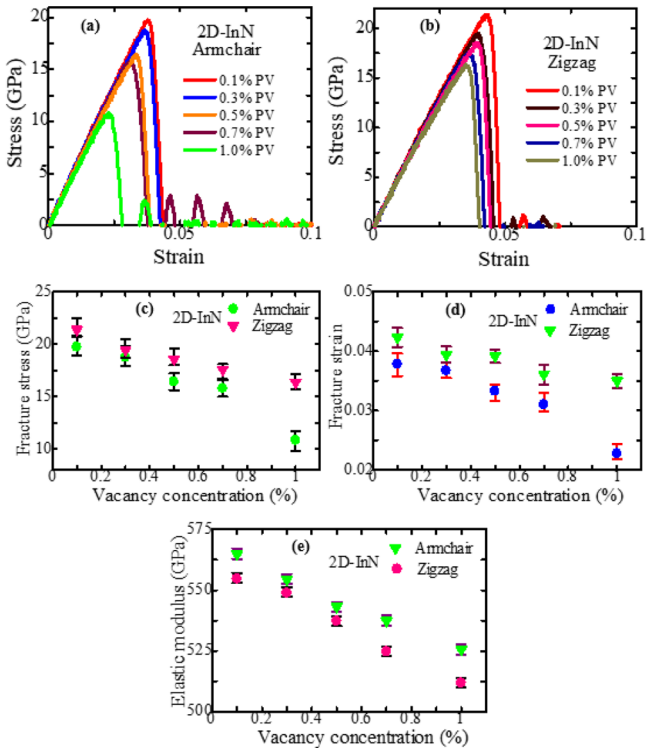

Figure 6. Stress−strain performances of PV-induced InN sheet at 300 K along the (a) armchair and (b) zigzag orientations. PV-induced (c) fracture stress, (d) fracture strain, and (e) elastic modulus of an InN sheet along the two different chiral orientations.

disordered GaN and InN monolayers with concentrations varying from 0.1 to 1.0%. For both chiral orientations, the stress−strain relationship depicts a linear pattern up to the fracture stress point, then a rapid deterioration, resulting in brittle fracture performance. As figures (Figures 5a,b and 6a,b) suggest, for both orientations, the critical fracture stress reveals a declining trend once the vacancy concentration is enhanced. For 0.1% PV-induced GaN, the evaluated fracture stress, elastic modulus, and fracture strain along the armchair orientation are found as ∼38.59 GPa, ∼682.03 GPa, and∼0.0629, respectively, while these values are ∼42.62 GPa, ∼679.31 GPa, and ∼0.0736, respectively, for the zigzag orientation. For 0.1% PV-induced InN, the evaluated fracture stress, elastic modulus, and fracture strain along the armchair orientation are found as ∼19.74 GPa, ∼564.87 GPa, and ∼0.0378, respectively, while these values are ∼21.38 GPa, ∼554.73 GPa, and ∼0.0423, respectively, for the zigzag orientation. The changes of mechanical properties with diverse concentrations of vacancy are revealed in Figures 5c,d and 6c,d. Due to the upsurge in the vacancy amount, both the fracture stress and strain decline monotonically. For a 1.0% PV concentration, the fracture stress of GaN is obtained as ∼33.28 GPa in the armchair direction, whereas it is ∼36.41 GPa in the zigzag direction. For the same vacancy concentration, the fracture stress of the InN is determined to be 10.85 and 16.37 GPa in the armchair and zigzag directions, respectively.

For both alignments, the change in the elastic modulus of XN with diverse vacancy densities is exposed in Figures 5e and 6e. It is perceived that for both alignments, the falling trend of elastic modulus is more considerable for the InN monolayer. At room temperature, owing to the integration of 1% PV into the InN configuration, the elastic modulus is reduced to ∼7.80 and ∼9.12% in the armchair and zigzag alignments, respectively, which is nearly 1.1−1.45 times superior to the declining trend of PV-provoked GaN. Islam et al.[21] and Jing et al.[51] also reported a similar type of elastic modulus decline for 2D-SiC and graphene with PV defects. The influence of PV concentration on the percentage decrease of different mechanical properties estimated for monolayer GaN and InN along the armchair and zigzag alignments are listed in Tables S5 and S6 (Supporting Information), respectively.

The change in the estimated mechanical behaviors of the single-layer XN comprising PV defect can be simply and qualitatively recognized from their potential energy per atom(PE/atom) calculation.[22,52−54] The PE/atom demonstrates a difference for diverse types of structures at zero strain. The difference should usually be the smallest for a perfect arrangement. Nevertheless, when the configuration comprises vacancy-ike defects, the PE/atom increases compared to the perfect case. For certain PV concentrations, as the structure is affected by a robust regularity failure effect than the perfect sheet, the PE/atom at zero strain should exhibit a greater value for the PV defected configuration. The evaluated PE/atom values for pristine, 0.1% PV, and 1.0% PV defects along the armchair and zigzag alignments of single-layer GaN and InN are shown in Figure 7a,b and 7c,d, respectively. From the figures, it can be perceived that for both chiral orientations, the unspoiled XN structure exposes a lesser initial PE/atom value compared to the PV-defected XN. Furthermore, the 1% PV-defected XN configuration reveals a greater initial PE/atom compared to the 0.1% PV-defected XN as a consequence of its greater regularity failure effect.

For a better understanding, the effects of increasing temperature and PV concentration, the stress distribution, and the deformation profile of XN at different strain levels are also explored here. For simplicity, here, we have only considered the armchair orientation of both GaN and InN monolayers. The temperature-dependent deformation profiles of GaN and InN are shown in Figures 8 and 9, respectively. The monolayer XN exhibits a superior stress value as the tensile strain increases. The void formation is first observed near the free ends of the sheet. The initial void formation and successive breakdown occur at nearly a comparable strain level, which proposes a brittle failure mechanism.

When the temperature is low, the number of damaged bonds is small for an identical strain value, as shown in Figures 8 and 9. However, for higher temperatures, the destruction of the bonding is so high that the sheet turned into fracture for a smaller strain value. The configuration undergoes essentially a minor thermal vibration at low temperatures and therefore the distortion and stress cannot be progressed quickly from the initial bond rupturing in the sheet to the whole configuration. However, at higher temperatures, as the thermal trembling effect is very high, the smaller strain level is enough to break the bond and create the void as well as damage the pristine sheet. The influence of temperature can be explicitly observed

https://doi.org/10.1021/acsomega.1c07259
ACS Omega 2022, 7, 14678−14689

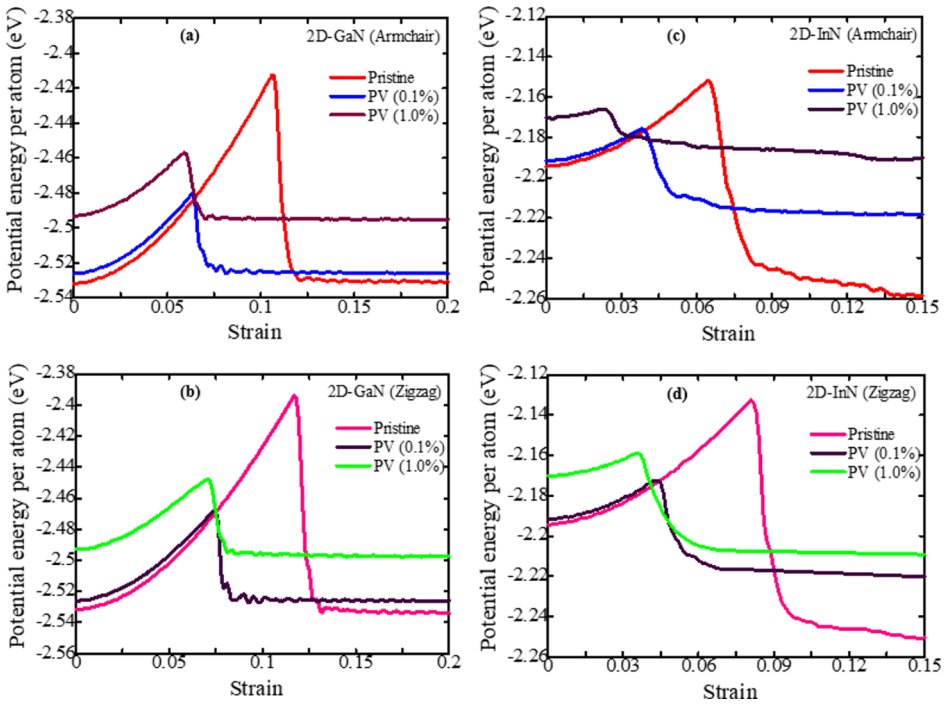

Figure 7. Effect of PV concentration on the PE/atom value of (a,b) GaN and (c,d) InN nanosheets along with the armchair and zigzag directions. Under zero strain conditions, the highest value of the PE/atom is obtained for the highest vacancy-induced structure.

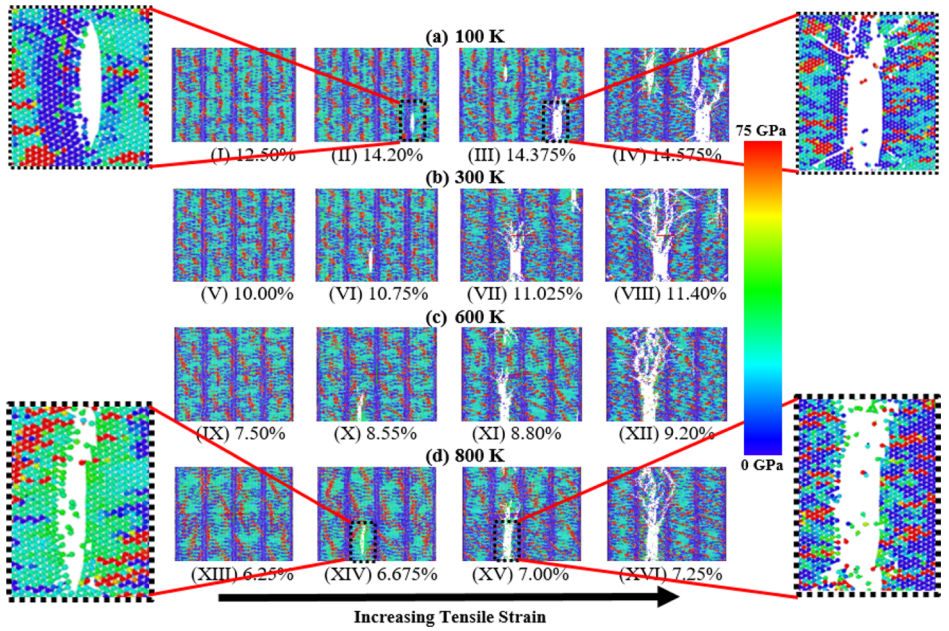

Figure 8. Tensile deformation profiles of a GaN nanosheet orientated in an armchair direction at (a) 100 K (I–IV), (b) 300 K (V–VIII), (c) 600 K (IX–XII) and (d) 800 K (XIII–XVI).

from the strain value at which the structure displays a failure. Besides, it is also observed that the fracture transmission occurs approximately 90° to the loading path for armchair-oriented pristine XN. Analogous crack promulgation is also revealed for other systems such as graphene, MoS_2, and *h*-BN nanosheets.[33,55]

The PV-induced XN shows a similar pattern of the growth of initial voids, the expansion of these empty spaces, and the final cracking of the sheet to that of pristine XN. As shown in Figures 10 and 11, the crack initiates from the vacancy site, and the pathway of crack propagation is along the vertical direction of the PV defects. In PV-induced XN, the initial debonding approves additional debonding of Ga and N as well as In and N atoms, which further origins an enormous amount of single atomic chains of Ga and N as well as In and N atoms and therefore leads to a configuration breaking. Similar to pristine XN, for PV-induced sheets, the initiation of void and development of the void is limited to a certain region, and the rest of the XN sheet remains nearly unaffected. Besides, for increasing PV concentration, the deformation starts at a significantly lower strain value compared to the lower

https://doi.org/10.1021/acsomega.1c07259
ACS Omega 2022, 7, 14678−14689

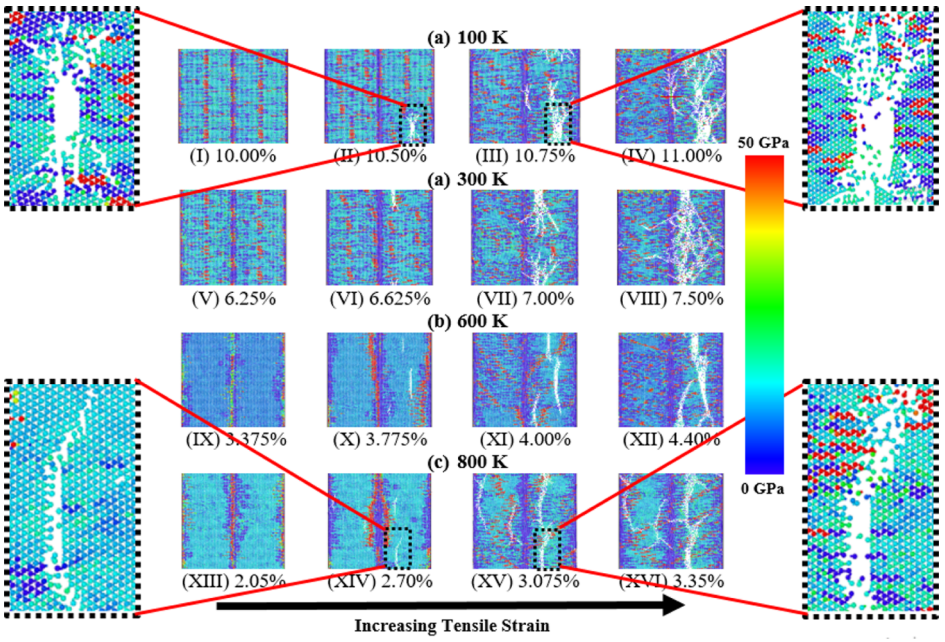

Figure 9. Tensile deformation profiles of a GaN nanosheet orientated in an armchair direction at (a) 100 K (I–IV), (b) 300 K (V–VIII), (c) 600 K (IX–XII), and (d) 800 K (XIII–XVI).

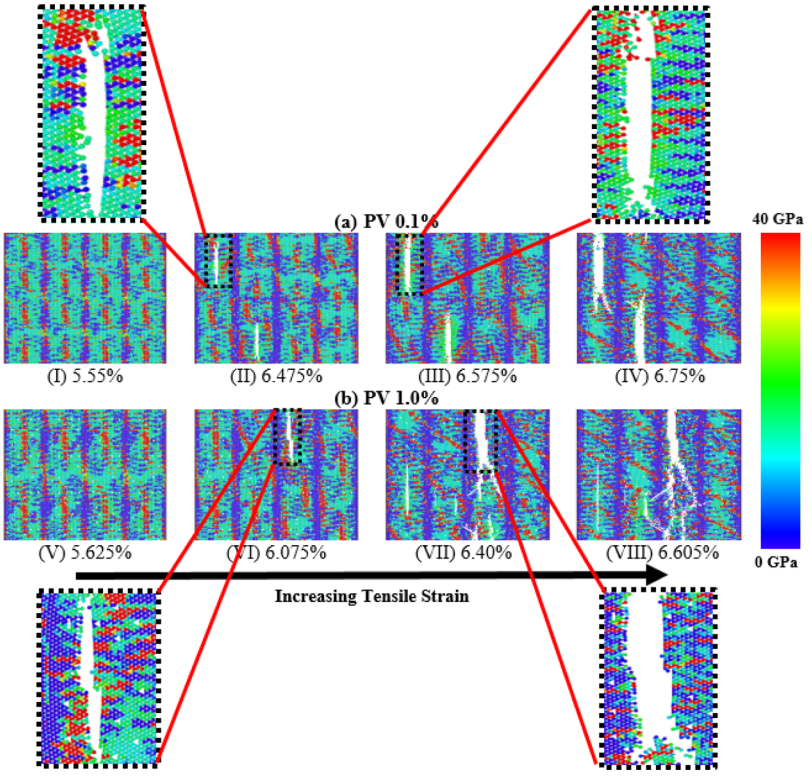

Figure 10. Tensile deformation profiles of an armchair-oriented GaN nanosheet at (a) PV 0.1% (I–IV) and (b) PV 1.0% (V–VIII).

concentration. This occurs due to the fact of the superior symmetry breakdown effect at higher concentrations of PV.

The fracture behavior of structural materials can be significantly altered for practical applications by varying the operational loading. Specifically, there is a significant difference in the tensile strength behavior as the strain rate is changed. At different strain rates, we examined the stress–strain correlation of XN. Figure 12a–d shows the stress–strain behaviors of both armchair and zigzag directed XN at various strain rates, including 1.5×10^{-3}, 1×10^{-3}, 3.5×10^{-4}, 2.1×10^{-4}, 5.5×10^{-5}, and 4.1×10^{-5} ps^{-1}. The fracture stress and corresponding fracture strain exhibit minor growing trends with increasing strain rates. Similar fracture behavior has been seen in a variety of materials, including 2D-SiGe, 2D-SiC, 2D-ZnS, and graphene.[21,22,24,25] Besides, the relationship between the fracture stress and the strain rate can be expressed by the Arrhenius equation as[21]

https://doi.org/10.1021/acsomega.1c07259
ACS Omega 2022, 7, 14678–14689

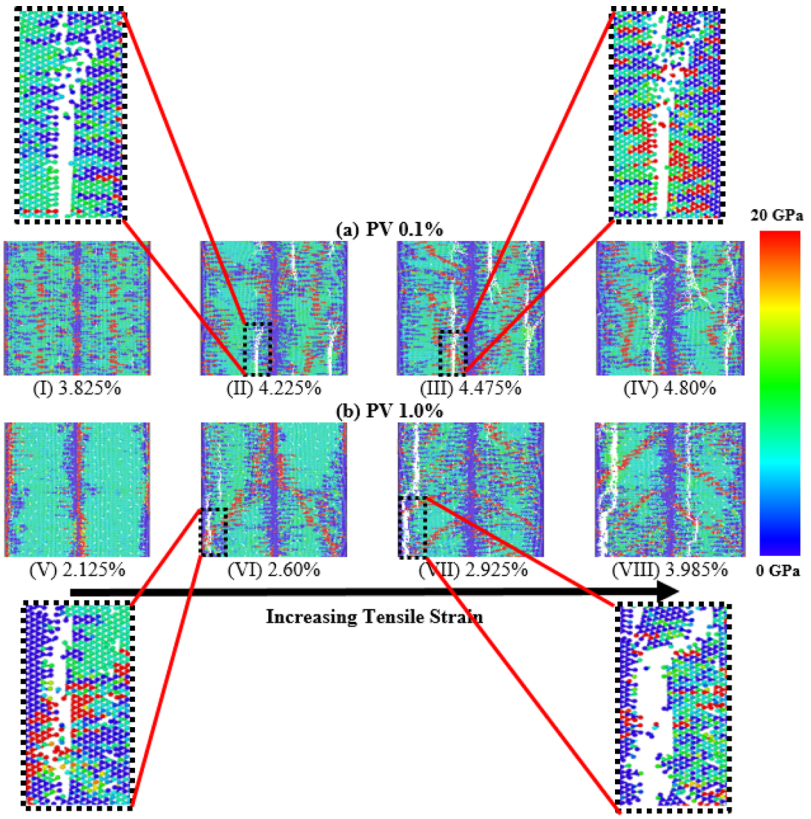

Figure 11. Tensile deformation profiles of an armchair-oriented InN nanosheet at (a) PV 0.1% (I–IV) and (b) PV 1.0% (V–VIII).

$$\dot{\varepsilon} = A\sigma^{1/m} \exp\left(\frac{-Q}{RT}\right) \tag{2}$$

where $\dot{\varepsilon}$ signifies the strain rate, σ signifies the fracture stress, Q signifies the activation energy, R is the universal gas constant, T is the deformation temperature, m is the strain-rate sensitivity, and A is a constant. Equation 2 can be further simplified by taking natural logarithms on both sides and assuming that temperature is constant during the deformation. Therefore, we can get

$$\ln \dot{\varepsilon} = \ln(A) + \frac{1}{m}\ln(\sigma) - \frac{Q}{RT} \tag{3}$$

Now, by calculating the slopes of ln (σ) and ln $(\dot{\varepsilon})$ profiles, the strain-rate sensitivity m can be obtained easily. The strain-rate sensitivity m is expressed as

$$m = \frac{\partial \ln(\sigma)}{\partial \ln(\dot{\varepsilon})} \tag{4}$$

The strain-rate sensitivity m for armchair- and zigzag-directed GaN is 0.023 and 0.0147, respectively, as shown in Figure 12e. Moreover, the strain-rate sensitivity is 0.042 and 0.0409 for armchair- and zigzag-directed InN, respectively (shown in Figure 12f). Therefore, the fracture stress of armchair-directed XN is more sensitive to the strain rate.

In addition to the strain rate effects, the size effect was investigated to ensure that the XN (X = Ga, In) structures employed in this study were large enough to produce size-independent results. The mechanical behaviors of two large GaN sheets with areas of 238.95 and 599.47 nm^2 and two InN sheets with areas of 222.15 and 617.25 nm^2 were examined. The explored fracture stress, strain, and elastic modulus of both GaN and InN with considered sheet area are illustrated in Figure S1 (Supporting Information). As we applied PBCs, the obtained mechanical properties of XN show size-independent results.

4.0. CONCLUSIONS

In conclusion, we studied the mechanical behavior of monolayer XN by using MD simulations. The influences of temperature (100 to 800 K) and PV defects (0.1 to 1.0% concentration) on the elastic modulus, fracture stress, and fracture strain of this XN monolayer were comprehensively analyzed. At room temperature, the computed fracture stresses of GaN were 59.52 and 61.41 GPa along the armchair and zigzag directions, respectively. Conversely, these values were 31.75 and 36.12 GPa, respectively, for InN. The mechanical strength of monolayer XN decreases as the system temperature increases and can be tuned by changing the PV concentrations. Introducing 1% PV can decrease the fracture stress of the monolayer GaN and InN by ∼(40−44) and ∼(56−65)%, respectively. To explain the obtained mechanical behavior quantitatively, the temperature-dependent RDF and PV-induced PE/atom were explored. The RDF peak exhibits a softening as well as broadening nature with increasing temperature, quantifying the reduction of mechanical strength at high temperatures. Among the different PV concentrations, the highest PE/atom at the zero strain level was recorded for a greater concentration of PVs verifying the vacancy-induced fracture behavior. The deformation profile for different temperatures demonstrates the stress distribution behavior at different strain levels, and increasing temperature shows an early breakdown of the sheet with a lower strain level. The atomic-scale simulations employed here will be beneficial for

https://doi.org/10.1021/acsomega.1c07259
ACS Omega 2022, 7, 14678−14689

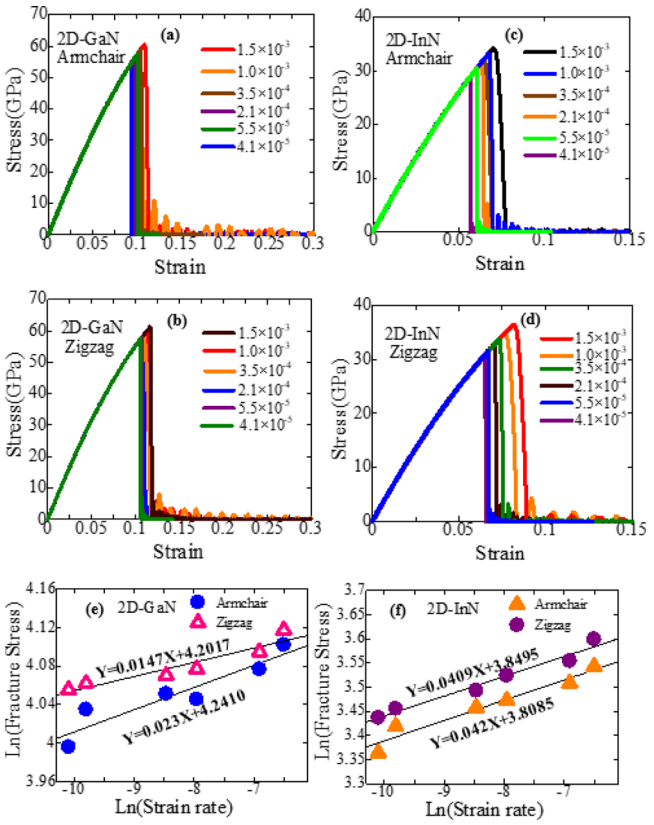

Figure 12. Strain−stress relationship of (a,b) GaN and (c,d) InN nanosheets along with the armchair and zigzag directions with different strain rates. The strain-rate sensitivity of (e) GaN and (f) InN nanosheets along the two chiral orientations.

understanding and accurately predicting the mechanical properties of monolayer XN as well as opening up new avenues toward rational defect engineering for advanced reliable device applications avoiding structural damaging.

■ ASSOCIATED CONTENT

Supporting Information

The Supporting Information is available free of charge at https://pubs.acs.org/doi/10.1021/acsomega.1c07259.

Comparison of different physical parameters of GaN and InN reported by MEAM potential in the MD simulation, experiments, and FP calculations; percentage reduction of diverse mechanical properties of 2D-GaN and 2D-InN along the armchair and zigzag directions at different temperatures; percentage reduction of diverse mechanical properties of 2D-GaN and 2D-InN along the armchair and zigzag directions at different PV concentrations; and effect of the sheet area on the stress−strain behavior of GaN and InN nanosheets along the armchair and zigzag directions (PDF)

■ AUTHOR INFORMATION

Corresponding Author

Md. Sherajul Islam − *Department of Electrical and Electronic Engineering, Khulna University of Engineering & Technology, Khulna 9203, Bangladesh; Department of Electrical and Biomedical Engineering, University of Nevada, Reno, Nevada 89557, United States;* orcid.org/0000-0002-6717-2523; Email: sheraj_kuet@eee.kuet.ac.bd

Authors

A. S. M. Jannatul Islam − *Department of Electrical and Electronic Engineering, Khulna University of Engineering & Technology, Khulna 9203, Bangladesh;* orcid.org/0000-0003-2101-6223

Md. Sayed Hasan − *Department of Electrical and Electronic Engineering, Khulna University of Engineering & Technology, Khulna 9203, Bangladesh*

Md. Shahadat Akbar − *Department of Electrical and Electronic Engineering, Khulna University of Engineering & Technology, Khulna 9203, Bangladesh;* orcid.org/0000-0001-6920-0981

Jeongwon Park − *School of Electrical Engineering and Computer Science, University of Ottawa, Ottawa ON K1N 6N5, Canada; Department of Electrical and Biomedical Engineering, University of Nevada, Reno, Nevada 89557, United States*

Complete contact information is available at: https://pubs.acs.org/10.1021/acsomega.1c07259

Author Contributions

A.S.M.J.I. contributed in conceptualization, methodology, software, investigation, and writing—original draft preparation. M.S.I. contributed in visualization, investigation, and writing—reviewing and editing. M.S.H. and M.S.A. contributed in software and data curation. J.P. contributed in supervision and writing—reviewing and editing.

Notes

The authors declare no competing financial interest.

■ ACKNOWLEDGMENTS

This study was supported by the facilities of the UGC funded research project (grant no. CASR-59/24, 2021−2022), provided by the CASR at Khulna University of Engineering & Technology, Bangladesh.

■ REFERENCES

(1) Androulidakis, C.; Zhang, K.; Robertson, M.; Tawfick, S. Tailoring the Mechanical Properties of 2D Materials and Heterostructures. *2D Materials* **2018**, *5*, 032005.

(2) Bonaccorso, F.; Colombo, L.; Yu, G.; Stoller, M.; Tozzini, V.; Ferrari, A. C.; Ruoff, R. S.; Pellegrini, V. Graphene, Related Two-Dimensional Crystals, and Hybrid Systems for Energy Conversion and Storage. *Science* **2015**, *347*, 1246501.

(3) Ekinci, K. L. Electromechanical Transducers at the Nanoscale: Actuation and Sensing of Motion in Nanoelectromechanical Systems (NEMS). *Small* **2005**, *1*, 786−797.

(4) Islam, M. S.; Mia, I.; Ahammed, S.; Stampfl, C.; Park, J. Exceptional In-Plane and Interfacial Thermal Transport in Graphene/2D-SiC van Der Waals Heterostructures. *Sci. Rep.* **2020**, *10*, 1−16.

(5) Rashid, A. S.; Islam, M. S.; Ferdous, N.; Anindya, K. N.; Park, J.; Hashimoto, A. Widely Tunable Electronic Properties in Graphene/Two-Dimensional Silicon Carbide van Der Waals Heterostructures. *J. Comput. Electron.* **2019**, *18*, 836−845.

(6) Lee, C.; Wei, X.; Kysar, J. W.; Hone, J. Measurement of the Elastic Properties and Intrinsic Strength of Monolayer Graphene. *Science* **2008**, *321*, 385−388.

(7) Zhao, H.; Aluru, N. R. Temperature and Strain-Rate Dependent Fracture Strength of Graphene. *J. Appl. Phys.* **2010**, *108*, 064321.

(8) Şahin, H.; Cahangirov, S.; Topsakal, M.; Bekaroglu, E.; Akturk, E.; Senger, R. T.; Ciraci, S. Monolayer Honeycomb Structures of Group-IV Elements and III-V Binary Compounds : First-Principles Calculations. *Phys. Rev. B: Condens. Matter Mater. Phys.* **2009**, *80*, 155453.

(9) Tian, J.; Liu, L.; Xia, S.; Diao, Y.; Lu, F. Optoelectronic Properties of Two-Dimensional GaN Adsorbed with H , N and O : A First-Principle Study. *Phys. Lett. A* **2019**, *383*, 3018−3024.
(10) Luo, Z.; Yang, Y.; Yang, X.; Lv, B.; Liu, X. The Mechanical Properties and Strain Effect on the Electronic Properties of III-Nitride Monolayers : Ab- Initio Study. *Mater. Res. Express* **2019**, *6*, 115915.
(11) Peng, Q.; Sun, X.; Wang, H.; Yang, Y.; Wen, X.; Huang, C.; Liu, S.; De, S. Theoretical Prediction of a Graphene-like Structure of Indium Nitride : A Promising Excellent Material for Optoelectronics. *Appl. Mater. Today* **2017**, *7*, 169−178.
(12) Qin, Z.; Qin, G.; Zuo, X.; Xiong, Z.; Hu, M. Orbitally Driven Low Thermal Conductivity of Monolayer Gallium Nitride (GaN) with Planar Honeycomb Structure: A Comparative Study. *Nanoscale* **2017**, *9*, 4295−4309.
(13) Sanders, N.; Bayerl, D.; Shi, G.; Mengle, K. A.; Kioupakis, E. Electronic and Optical Properties of Two-Dimensional GaN from First Principles. *Nano Lett.* **2017**, *17*, 7345−7349.
(14) Sankaranarayanan, S.; Kandasamy, P.; Raju, R.; Krishnan, B. Fabrication of Gallium Nitride and Nitrogen Doped Single Layer Graphene Hybrid Heterostructures for High Performance Photodetectors. *Sci. Rep.* **2020**, *10*, 1−12.
(15) Wu, K.; Huang, S.; Wang, W.; Li, G. Recent Progress in III-Nitride Nanosheets: Properties, Materials and Applications. *Semicond. Sci. Technol.* **2021**, *36*, 123002.
(16) Al Balushi, Z. Y.; Wang, K.; Ghosh, R. K.; Vilá, R. A.; Eichfeld, S. M.; Caldwell, J. D.; Qin, X.; Lin, Y.-C.; Desario, P. A.; Stone, G.; Subramanian, S.; Paul, D. F.; Wallace, R. M.; Datta, S.; Redwing, J. M.; Robinson, J. A. Two-Dimensional Gallium Nitride Realized via Graphene Encapsulation. *Nat. Mater.* **2016**, *15*, 1166−1171.
(17) Syed, N.; Zavabeti, A.; Messalea, K. A.; Della Gaspera, E.; Elbourne, A.; Jannat, A.; Mohiuddin, M.; Zhang, B. Y.; Zheng, G.; Wang, L.; Russo, S. P.; Esrafilzadeh, D.; McConville, C. F.; Kalantar-Zadeh, K.; Daeneke, T. Wafer-Sized Ultrathin Gallium and Indium Nitride Nanosheets through the Ammonolysis of Liquid Metal Derived Oxides. *J. Am. Chem. Soc.* **2019**, *141*, 104−108.
(18) Chen, Y.; Liu, K.; Liu, J.; Lv, T.; Wei, B.; Zhang, T.; Zeng, M.; Wang, Z.; Fu, L. Growth of 2D GaN Single Crystals on Liquid Metals. *J. Am. Chem. Soc.* **2018**, *140*, 16392−16395.
(19) Gautam, A.; Van Veggel, F. C. J. M. Synthesis of InN@SiO 2 Nanostructures and Fabrication of Blue LED Devices. *ACS Appl. Mater. Interfaces* **2012**, *4*, 3902−3909.
(20) Islam, M. S.; Zamil, M. Y.; Mojumder, M. R. H.; Stampfl, C.; Park, J. Strong Tribo-Piezoelectric Effect in Bilayer Indium Nitride (InN). *Sci. Rep.* **2021**, *11*, 1−12.
(21) Islam, A. S. M. J.; Islam, M. S.; Ferdous, N.; Park, J.; Bhuiyan, A. G.; Hashimoto, A. Anisotropic Mechanical Behavior of Two Dimensional Silicon Carbide: Effect of Temperature and Vacancy Defects. *Mater. Res. Express* **2019**, *6*, 125073.
(22) Islam, A. S. M. J.; Hasan, M. S.; Islam, M. S.; Park, J. Chirality, Temperature, and Vacancy Effects on Mechanical Behavior of Monolayer Zinc-Sulfide. *Comput. Mater. Sci.* **2021**, *200*, 110824.
(23) Wang, X.; Hong, Y.; Wang, M.; Xin, G.; Yue, Y.; Zhang, J. Mechanical Properties of Molybdenum Diselenide Revealed by Molecular Dynamics Simulation and Support Vector Machine. *Phys. Chem. Chem. Phys.* **2019**, *21*, 9159−9167.
(24) Islam, A. S. M. J.; Akbar, M. S.; Islam, M. S.; Park, J. Temperature- and Defect-Induced Uniaxial Tensile Mechanical Behaviors and the Fracture Mechanism of Two-Dimensional Silicon Germanide. *ACS Omega* **2021**, *6*, 21861−21871.
(25) Zhang, Y.-Y.; Pei, Q.-X.; Mai, Y.-W.; Gu, Y.-T. Temperature and Strain-Rate Dependent Fracture Strength of Graphynes. *J. Phys. D: Appl. Phys.* **2014**, *47*, 425301.
(26) Li, N.; Ding, N.; Qu, S.; Liu, L.; Guo, W.; Wu, C.-M. L. Mechanical Properties and Failure Behavior of Hexagonal Boron Nitride Sheets with Nano-Cracks. *Comput. Mater. Sci.* **2017**, *140*, 356−366.
(27) Gao, Y.; Sun, D.; Jiang, X.; Zhao, J. Point Defects in Group III Nitrides: A Comparative First-Principles Study. *J. Appl. Phys.* **2019**, *125*, 215705.
(28) Diallo, I. C.; Demchenko, D. O. Native Point Defects in GaN: A Hybrid-Functional Study. *Phys. Rev. Appl.* **2016**, *6*, 064002.
(29) Lyons, J. L.; Wickramaratne, D.; Van De Walle, C. G. A First-Principles Understanding of Point Defects and Impurities in GaN. *J. Appl. Phys.* **2021**, *129*, 111101.
(30) Ganchenkova, M. G.; Nieminen, R. M. Nitrogen Vacancies as Major Point Defects in Gallium Nitride. *Phys. Rev. Lett.* **2006**, *96*, 196402.
(31) Islam, A. S. M. J.; Islam, M. S.; Ferdous, N.; Park, J.; Hashimoto, A. Vacancy-Induced Thermal Transport in Two-Dimensional Silicon Carbide: A Reverse Non-Equilibrium Molecular Dynamics Study. *Phys. Chem. Chem. Phys.* **2020**, *22*, 13592−13602.
(32) Zandiatashbar, A.; Lee, G.-H.; An, S. J.; Lee, S.; Mathew, N.; Terrones, M.; Hayashi, T.; Picu, C. R.; Hone, J.; Koratkar, N. Effect of Defects on the Intrinsic Strength and Stiffness of Graphene. *Nat. Commun.* **2014**, *5*, 1−9.
(33) Mahata, A.; Jiang, J.-W.; Mahapatra, D. R.; Rabczuk, T. Effect of Intrinsic Structural Defects on Mechanical Properties of Single Layer MoS 2. *Nano-Struct. Nano-Objects* **2019**, *18*, 100247.
(34) Eshkalak, K. E.; Sadeghzadeh, S.; Jalaly, M. Mechanical Properties of Defective Hybrid Graphene-Boron Nitride Nanosheets: A Molecular Dynamics Study. *Comput. Mater. Sci.* **2018**, *149*, 170−181.
(35) Islam, A. S. M. J.; Islam, M. S.; Mim, N. Z.; Akbar, M. S.; Hasan, M. S.; Islam, M. R.; Stampfl, C.; Park, J. Vacancy-Induced Thermal Transport and Tensile Mechanical Behavior of Monolayer Honeycomb BeO. *ACS Omega* **2022**, *7*, 4525−4537.
(36) Sun, X.; Yang, Q.; Meng, R.; Tan, C.; Liang, Q.; Jiang, J.; Ye, H.; Chen, X. Adsorption of Gas Molecules on Graphene-like InN Monolayer : A First-Principle Study. *Appl. Surf. Sci.* **2017**, *404*, 291−299.
(37) Prete, M. S.; Pulci, O.; Bechstedt, F. Strong in- and out-of-Plane Excitons in Two-Dimensional InN Nanosheets. *Phys. Rev. B: Condens. Matter Mater. Phys.* **2018**, *98*, 235431.
(38) Farzaneh, G.; Faramarz, K. Strain Effect on the Electronic Properties of III-Nitride Nanosheets : Ab-Initio Study. *Sci. China: Technol. Sci.* **2018**, *61*, 535−541.
(39) Das, A.; Yadav, R. K. Electronic and Vibrational Properties of Pristine and Cd, Si, Zn and Ge-Doped InN Nanosheet: A First Principle Study. *Struct. Chem.* **2021**, *32*, 379−386.
(40) Prete, M. S.; Mosca Conte, A.; Gori, P.; Bechstedt, F.; Pulci, O.; Pulci, O. Tunable Electronic Properties of Two- Dimensional Nitrides for Light Harvesting Heterostructures. *Appl. Phys. Lett.* **2017**, *110*, 012103.
(41) Alaal, N.; Roqan, I. S. Tuning the Electronic Properties of Hexagonal Two-Dimensional GaN Monolayers via Doping for Enhanced Optoelectronic Applications. *ACS Appl. Nano Mater.* **2018**, *2*, 202−213.
(42) Li, Z.-w.; Guo, D.-p.; Huang, G.-y.; Tao, W.-l.; Duan, M.-y. Electronic Structures and Optical Properties of Ga Doped Single-Layer Indium Nitride Electronic Structures and Optical Properties of Ga Doped Single-Layer. *Chin. J. Chem. Phys.* **2018**, *31*, 313.
(43) Do, E. C.; Shin, Y.-H.; Lee, B.-J. Atomistic Modeling of III − V Nitrides : Modified Embedded-Atom Method Interatomic Potentials for GaN , InN and Ga 1 − x In x N. *J. Phys.: Condens. Matter* **2009**, *21*, 325801.
(44) Tsai, D. H. The Virial Theorem and Stress Calculation in Molecular Dynamics. *J. Chem. Phys.* **1979**, *70*, 1375−1382.
(45) Stukowski, A. Visualization and Analysis of Atomistic Simulation Data with OVITO-the Open Visualization Tool. *Modell. Simul. Mater. Sci. Eng.* **2010**, *18*, 015012.
(46) Hassan, A.; Savaria, Y.; Sawan, M. GaN Integration Technology, an Ideal Candidate for High-Temperature Applications: A Review. *IEEE Access* **2018**, *6*, 78790−78802.
(47) Pearton, S. J.; Ren, F.; Zhang, A. P.; Dang, G.; Cao, X. A.; Lee, K. P.; Cho, H.; Gila, B. P.; Johnson, J. W.; Monier, C.; Abernathy, C. R.; Han, J.; Baca, A. G.; Chyi, J. I.; Lee, C. M.; Nee, T. E.; Chuo, C. C.; Chu, S. N. G. GaN Electronics for High Power, High Temperature Applications. *Mater. Sci. Eng., B* **2001**, *82*, 227−231.

https://doi.org/10.1021/acsomega.1c07259
ACS Omega 2022, 7, 14678−14689

(48) Mohanty, S. K.; Chen, Y.-Y.; Yeh, P.-H.; Horng, R.-H. Thermal Management of GaN-on-Si High Electron Mobility Transistor by Copper Filled Micro-Trench Structure. *Sci. Rep.* **2019**, *9*, 1−9.
(49) Werner, M. R.; Fahrner, W. R. Review on Materials, Microsensors, Systems, and Devices for High-Temperature and Harsh-Environment Applications. *IEEE Trans. Ind. Electron.* **2001**, *48*, 249−257.
(50) Pérez-Tomás, A.; Placidi, M.; Baron, N.; Chenot, S.; Cordier, Y.; Moreno, J. C.; Constant, A.; Godignon, P.; Millán, J. GaN Transistor Characteristics at Elevated Temperatures. *J. Appl. Phys.* **2009**, *106*, 74519.
(51) Jing, N.; Xue, Q.; Ling, C.; Shan, M.; Zhang, T.; Zhou, X.; Jiao, Z. Effect of Defects on Young's Modulus of Graphene Sheets: A Molecular Dynamics Simulation. *RSC Adv.* **2012**, *2*, 9124−9129.
(52) Lu, Q.; Gao, W.; Huang, R. Atomistic Simulation and Continuum Modeling of Graphene Nanoribbons under Uniaxial Tension. *Modell. Simul. Mater. Sci. Eng.* **2011**, *19*, 054006.
(53) Sun, Y. J.; Huang, Y. H.; Ma, F.; Ma, D. Y.; Hu, T. W.; Xu, K. W. Molecular Dynamics Simulation on Double-Elastic Deformation of Zigzag Graphene Nanoribbons at Low Temperature. *Mater. Sci. Eng. B: Solid-State Mater. Adv. Technol.* **2014**, *180*, 1−6.
(54) Islam, A. S. M. J.; Akbar, M. S.; Islam, M. S.; Park, J. Temperature- and Defect-Induced Uniaxial Tensile Mechanical Behaviors and the Fracture Mechanism of Two-Dimensional Silicon Germanide. *ACS Omega* **2021**, *6*, 21861−21871.
(55) Mortazavi, B.; Ahzi, S. Thermal Conductivity and Tensile Response of Defective Graphene: A Molecular Dynamics Study. *Carbon* **2013**, *63*, 460−470.

https://doi.org/10.1021/acsomega.1c07259
ACS Omega 2022, 7, 14678−14689